# 48-spot single-molecule FRET setup with periodic acceptor excitation

Antonino Ingargiola,[1, a)] Maya Segal,[1] Angelo Gulinatti,[2] Ivan Rech,[2] Ivan Labanca,[2] Piera Maccagnani,[3] Massimo Ghioni,[2] Shimon Weiss,[1] and Xavier Michalet[1, b)]

[1)] *Dept. Chemistry and Biochemistry, University of California Los Angeles, USA*

[2)] *DEIB, Politecnico di Milano, Italy*

[3)] *Istituto per la Microelettronica e Microsistemi, IMM-CNR, Bologna, Italy.*

(Dated: June 26, 2017)

Single-molecule FRET (smFRET) allows measuring distances between donor (D) and acceptor (A) fluorophores on the 3-10 nm range. Solution-based smFRET allows measurement of binding-unbinding events or conformational changes of dye-labeled biomolecules without ensemble averaging and free from surface perturbations. When employing dual (or multi) laser excitation, smFRET allows resolving the number of fluorescent labels on each molecule, greatly enhancing the ability to study heterogeneous samples. A major drawback to solution-based smFRET is the low throughput, which renders repetitive measurements expensive and hinders the ability to study kinetic phenomena in real-time.

Here we demonstrate a high-throughput smFRET system which multiplexes acquisition by using 48 excitation spots and two 48-pixel SPAD array detectors. The system employs two excitation lasers allowing separation of species with one or two active fluorophores. The performance of the system is demonstrated on a set of doubly-labeled double-stranded DNA oligonucleotides with different distances between D and A dyes along the DNA duplex. We show that the acquisition time for accurate subpopulation identification is reduced from several minutes to seconds, opening the way to high-throughput screening applications and real-time kinetics studies of enzymatic reactions such as DNA transcription by bacterial RNA polymerase.

Keywords: Single-molecule FRET, high-throughput, SPAD array

## I. INTRODUCTION

Detailed knowledge of the three-dimensional (3D) atomistic structure of macromolecular complexes is essential to understand their biological function. For decades, X-ray crystallography and nuclear magnetic resonance (NMR) spectroscopy have been the techniques of choice for obtaining atomically resolved macromolecular structures. More recently, single-particle cryo-electron microscopy (cryo-EM) has complemented these methods for determination of large macromolecular structures with the added ability to classify different conformations. However, macromolecules spontaneously and dynamically explore various conformations in equilibrium that are hard to capture by the above-mentioned methods. Understanding the functional roles of these structures requires a full dynamic picture. Single-molecule Förster resonance energy transfer (smFRET) has paved the way for studying such structural dynamics in biologically-relevant conditions. smFRET allows determination of each conformational state that may exist in an ensemble of macromolecular complexes as well as the distance between specific residues for each state[1–4]. Recently, several groups used smFRET to measure distances between multiple different pairs of residues to construct 3D macromolecular structures of distinct conformations by triangulation and comparison to existing X-ray crystal structures[5–10]. Moreover, smFRET can measure the time-evolution of various distances between multiple FRET pairs, and hence report upon the dynamic 3D structure of a macromolecule undergoing conformational changes. Thus far, due to the requirement of low sample concentration imposed by the necessity to have no more than one molecule within the diffraction-limited confocal volume at a given time[1,11], only very slow kinetics can be measured. Therefore, increased throughput is essential for both static and dynamic measurements of multiple distances.

To overcome this limitation, we recently introduced a multispot excitation scheme taking advantage of novel single-photon avalanche diode (SPAD) arrays[12–14]. We demonstrated that the resulting setup indeed allowed acquisition of single-molecule data comparable to that of standard single-spot setups, but with a throughput that scaled with the number of excitation spots. We illustrated an application of this enhanced throughput by measuring the bubble closing kinetics during promoter escape in bacterial transcription[14]. While encouraging, these results were partially unsatisfactory because they were obtained with only 8 spots, and also because the setup only incorporated a single laser, used for excitation of the donor (D) dye of the FRET donor-acceptor (D-A) pair[14]. Single-laser smFRET is unable to distinguish between low FRET molecules (molecules with two active D and A dyes in which the D-A distance is large compared to the characteristic FRET length scale) from D-only molecules (i.e. molecules with a single D-dye, or dually-labeled molecules with an inactivated or bleached A-dye). Since the latter categories are present in most samples, it is important to identify and separate them from low FRET molecules of interest.

To address this problem, *Microsecond Alternated Laser*

[a)] Electronic mail: ingargiola.antonino@gmail.com

[b)] Electronic mail: michalet@chem.ucla.edu

*EXcitation* smFRET (referred throughout as µsALEX for brevity), was introduced several years ago[15], and later extended to pulsed laser excitation schemes (nsALEX[16] or PIE[17]). Briefly, in µsALEX, two exciting lasers are alternately turned on and off every few tens of µs allowing the separation of species with only a single active dye (D-only, A-only populations) from doubly-labeled species with both dyes active (FRET population). In fact, only FRET populations give a fluorescence signal both during the D-laser excitation due to excitation of the D-dye and the A-laser excitation due to excitation of the A-dye. This, in turn, extends the number of FRET subpopulations that can be possibly identified within a sample in the regime of low mean FRET efficiencies. This scheme has since been extended to 3 or 4 laser excitations, allowing powerful molecular sorting applications[18,19]. A simplified version of this laser alternation principle was presented in ref. 20, where the D-excitation laser is left on at all times while the A-laser is alternated. This periodic acceptor excitation single-molecule FRET technique[20] (referred to as PAX for brevity) allows simplifying the optical setup while maintaining the advantages of µsALEX, namely the ability to determine the stoichiometry of D and A dyes on each single molecule or to identify changes in the fluorescence quantum yields[21]. Here we present a significant improvement to our original multispot setup by (i) introducing a 48-spot illumination and detection scheme, and (ii) implementing a 2-laser PAX illumination approach.

This paper is organized as follows. In section II we briefly introduce the optical setup, the detectors (section II A) and the modulation scheme (section II B). In section III we report single-molecule measurements, starting with a brief description of the data analysis (section III A). To demonstrate the uniformity across channels, for each spot we report the peak photon rate in bursts (section III B) and E-S histograms (section III C). Finally, in section III D we present a comparison of single-spot µsALEX and 48-spot PAX measurements for a 15 second acquisition.

### A. Software and data availability

Software needed to operate the multispot setup (including LCOS-SLM pattern generation, LabVIEW-FPGA timestamping code, piezo-motor control, etc.) is organized in different repositories and available on GitHub at https://github.com/multispot-software. Software used for data analysis in this paper can be found in the 48-spot-smFRET-PAX-analysis repository. Links to specific notebooks are added in the caption of each figure. Data files are publicly available on Figshare[22].

## II. SETUP DESCRIPTION

In this section, we outline a brief description of the setup. A more detailed description can be found in appendix A, while details of laser and SPAD array alignment can be found in appendix B and C respectively.

A schematic of the setup is reported in Fig. 1. The setup includes two 1W CW excitation laser (green: 532 nm, red: 628 nm) with only the red laser being modulated via an acoustic-optic modulator (AOM). After polarization adjustment and beam expansion, the two lasers are phase modulated by the respective LCOS-SLM generating two 48-spots patterns on a plane after each LCOS-SLM (*LCOS image plane*). The two lasers are then combined by a dichroic mirror ($DM_{MIX}$) and recollimated ($L_3$) before being focused into the sample by an high numerical aperture (NA) objective lens (60x, NA=1.2). Emitted fluorescence is collected by the same objective lens, separated by excitation wavelength through a dual-band polychroic mirror ($DM_{EX}$), and focused by a tube lens ($L_2$) into the image plane. Next, emitted fluorescence light is recollimated ($L_4$), separated into donor and acceptor spectral bands ($DM_{EM}$), and focused into two different 48-pixel SPAD arrays that are mounted on motorized micro-positioning stages. The system is aligned so that each SPAD pixel is optically conjugated to one excitation spot into the sample.

Output from the detectors is processed by an FPGA-based board which performs photon timestamping with 12.5 ns resolution and transfers data to a host PC. The host PC runs an acquisition software that displays 96-channel timetraces in real-time, implements alignment routines, and saves the acquisition to disk. Further data conversion and analysis is performed on a second PC.

### A. Detectors

The current 48-spot setup employs two identical 12x4-pixel SPAD arrays whose architecture and performance has been presented in 23. Here we describe only the most salient features. The active area of each pixel has a 50 µm diameter. The array is comprised by 4 rows of 12 pixels (4x12) with a 500 µm pitch in each direction.

To easily integrate the detectors into a multispot setup, we developed a photon-counting module that integrates a 48-pixel SPAD array and the electronics required for device operation, data acquisition, and transmission into a compact, user friendly module. In particular, the SPAD array is housed into a hermetically sealed chamber separated from the rest of the module. Sealing in a dry atmosphere makes it possible to mount the array on a double-stage Peltier, cooling the detector down to temperatures of approximately −15°C and thereby reducing the dark count rate (DCR) and increasing the sensitivity of the instrument. Photon-counting pulses are made externally available through a standard SCSI connector. This allows for an easy connection of the module to general-purpose boards for data acquisition and processing. Alternatively, an onboard FPGA (Spartan 6 SLX150, Xilinx, San Jose, CA, USA) can be used to time-stamp counts detected in each of the 48-channels with a time resolution of 10 ns where this information is sent to a remote PC through a high-speed USB link. A C-mount at the top of the photon-counting module allows for easy and reliable connections to the multispot setup.

The two SPAD arrays used in the current 48-spot

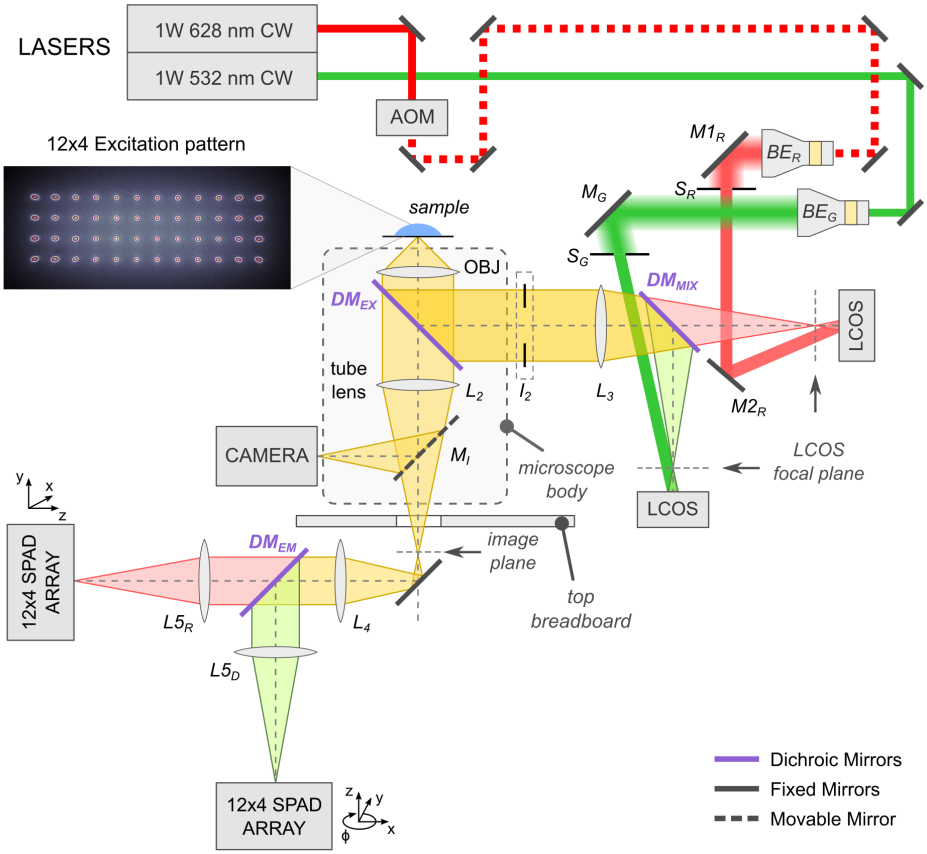


Figure 1. Schematic of the 48-spot smFRET-PAX setup. See man text and appendix A for a detailed description.

smFRET-PAX setup are operated at a temperature of -10 °C. The photon detection efficiency (PDE) reaches a maximum of ~45% at 550 nm and drops to 35% at 628nm[23,24]. The PDE is highly uniform over the array, with a peak-to-peak spread of only a few percent. Fig. 2 shows heatmaps of dark count rates for the two 12x4 SPAD arrays. About 80% of the pixels have a DCR lower than 1000 counts per second (cps), whereas the worst performing pixel has a fairly low DCR of less than 6 kcps.

48-spot smFRET-PAX results were compared to the state-of-the-art single-spot µsALEX setup previously described in 14. This setup employs two single-pixel commercial SPADs (SPCM-AQRH, Excelitas Technology Corp., Waltham, MA, USA) characterized by PDE similar to our SPAD arrays in the D spectral band but with a more than two-fold higher PDE in the A spectral band. For this reason, the µsALEX setup is expected to be at least twice as sensitive in the A-channel than the 48-spot setup. A detailed comparison of the different SPAD technologies for single-molecule measurements is reported in 24.

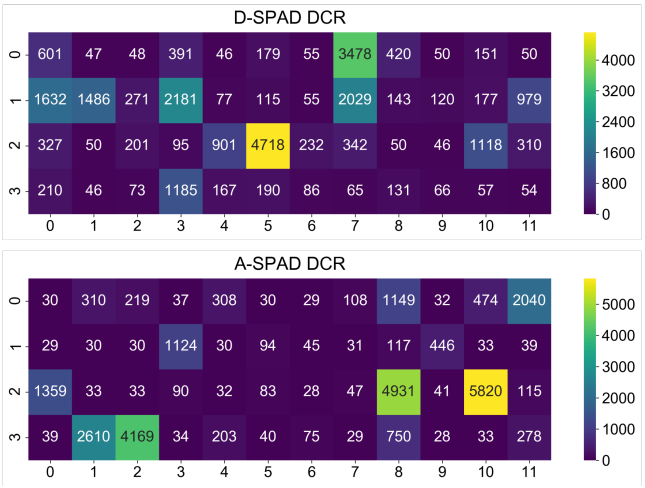


Figure 2. Heatmaps of dark count rates (DCR) for the 12x4 D and A SPAD arrays used in the current 48-spot smFRET-PAX setup. DCR values are overlaid on each pixel. All values are in counts per second (cps). More details and data underlying this figure can be found in the notebook DCR plots.

### B. 48-spot pattern

The 48 excitation spots are generated independently for each wavelength by phase modulation of an incoming plane wave, as previously described in 14 and 25. The phase modulation operates in direct space rather than Fourier space and implements the phase profile of a Fresnel lenslet array. Delon's groups employed a conceptually similar direct-space modulation scheme using an LCOS-SLM for multi-confocal fluorescence correla-

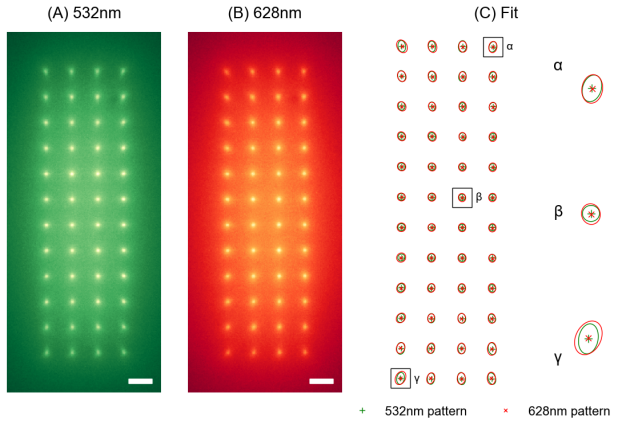


Figure 3. The 12x4 multispot pattern for green (A) and red (B) excitation and Gaussian fit of the spots (C). The pattern is acquired by a camera on the microscope side port (see Fig. 1) using a solution of ATTO550 and ATTO647N dyes at high concentration (∼100 nM). Fluorescent images obtained upon 532 nm or 628 nm laser excitation were acquired separately and are reported in green and red intensity levels in panels (A) and (B), respectively. Scale bars are 5 µm. To assess the alignment, each spot in the two images is fitted with a 2D Gaussian function. Panel (C) reports an overlay of the fitted peak positions and a contour of the Gaussian waist for 532 nm (*green*) and 628 nm (*red*) images. A zoom-in for 3 representative spots is reported on the right. The elliptical shape and rotation of the Gaussian is due to geometrical aberrations. More details can be found in the notebook LCOS pattern fitting-conf9_G_conf14_R_4x12_slits.

tion spectroscopy (FCS)[26] (although they use a different spatial arrangement of the phase pattern on the LCOS-SLM).

Fig. 3 shows the emission pattern due to the green (Panel A) and red lasers (Panel B) acquired by a camera on the microscope side-port using a high-concentration dye sample. The two patterns are aligned to maximize overlap of each of the 48 spots. Overlap of the two wavelengths and centering with respect to the optical axis is assessed via 2-D Gaussian fitting as reported in Panel C. Full details on the alignment procedure and pattern assessment can be found in appendix A 1.

## III. SMFRET MEASUREMENTS

### A. Analysis

Single-molecule measurements were performed with 40 base-pair (bp) dsDNA samples labeled with dyes ATTO550 (D) and ATTO647N (A) (ATTOTEC GmbH, Heidelberg, Germany) attached to different DNA bases, yielding different inter-dye distances.

D-A separation of 12 and 22 base pairs (bp) were used in these experiments, as they cover the typical range of distances that can be accurately measured with smFRET using this dye pair. Samples were diluted to single-molecule concentration (∼ 50 pM) in TE50 buffer (10 mM Tris pH 8.0, 1 mM EDTA, and 50 mM NaCl). Full details regarding these samples are provided in ref. 14.

We analyzed data using standard µsALEX methods[21] with modifications required for smFRET-PAX[20]. The three steps of the analysis are: (a) background estimation, (b) burst search, and (c) burst selection. Background estimation, which is used to correct the burst counts in the different photon streams, was performed in 10 s time windows in order to account for possible variations during the measurement. Burst searches were performed independently for each spot using the sliding-window algorithm[11] and a constant-rate threshold for all spots[27].

The main result of the µsALEX analysis is a so-called E-S histogram, a two-dimensional histogram where each burst is represented by a pair of values $(E, S)$. $E$ is either the FRET efficiency or, more commonly the uncorrected FRET efficiency, known as proximity ratio, $E_{PR}$. $E_{PR}$ is easier to compute and provides a suitable approximation for identifying sub-populations. However, when the purpose is to extract D-A distances (which is not the objective of this study), $E$ must be computed, requiring accurate estimation of all the correction coefficients. $S$ is the "stoichiometry ratio," a quantity ideally centered around 0.5 for doubly-labeled species, 0 for A-only, and 1 for D-only species. Note that D and A-only species also include doubly-labeled molecules where one dye is fluorescently inactive either in the blinking off state or bleached. When using the simpler version without correction (eq. D8), $S$ can depend on $E$ and, for doubly-labeled molecules is only approximately centered around 0.5. The use of the $(E, S)$ pair (corrected or uncorrected) allows separation of singly and doubly-labeled species and distinguishing FRET sub-populations in the doubly-labeled population. Definition of all these quantities and a comparison with their ALEX counterpart is reported in the appendix D.

In this paper, we report proximity ratios $E_{PR}$ computed according to eq. D6, and a "modified stoichiometry ratio" $S_u$ defined in eq. D19. $S_u$ is a variant of the classical smFRET-PAX stoichiometry[20], which reduces the effect of shot noise and improves the separability of D-only and FRET populations. More details on $S_u$ can be found in appendix D 1. Note that throughout this work the results of the two leftmost spots in the second row are missing because of an active quenching circuit (AQC) failure in the D-SPAD array.

### B. Peak photon rate

We start by analyzing the peak photon rate reached in each burst, a quantity that scales with peak PSF intensity[14]. Fig. 4 shows the background-corrected peak photon-rate in each burst for the 48 spots. Panel A shows the full peak photon-rate distributions with their characteristic exponential tails. Panels B-E show heatmaps for different photon streams of the peak photon-rate mean values i.e. the decay constant of the exponential tail. Due to the Gaussian profile of the excitation beam and to geometrical aberrations, the lateral pixels receive a lower signal intensity than central pixels. As a result, the peak photon-rate decreases and fewer single-molecule

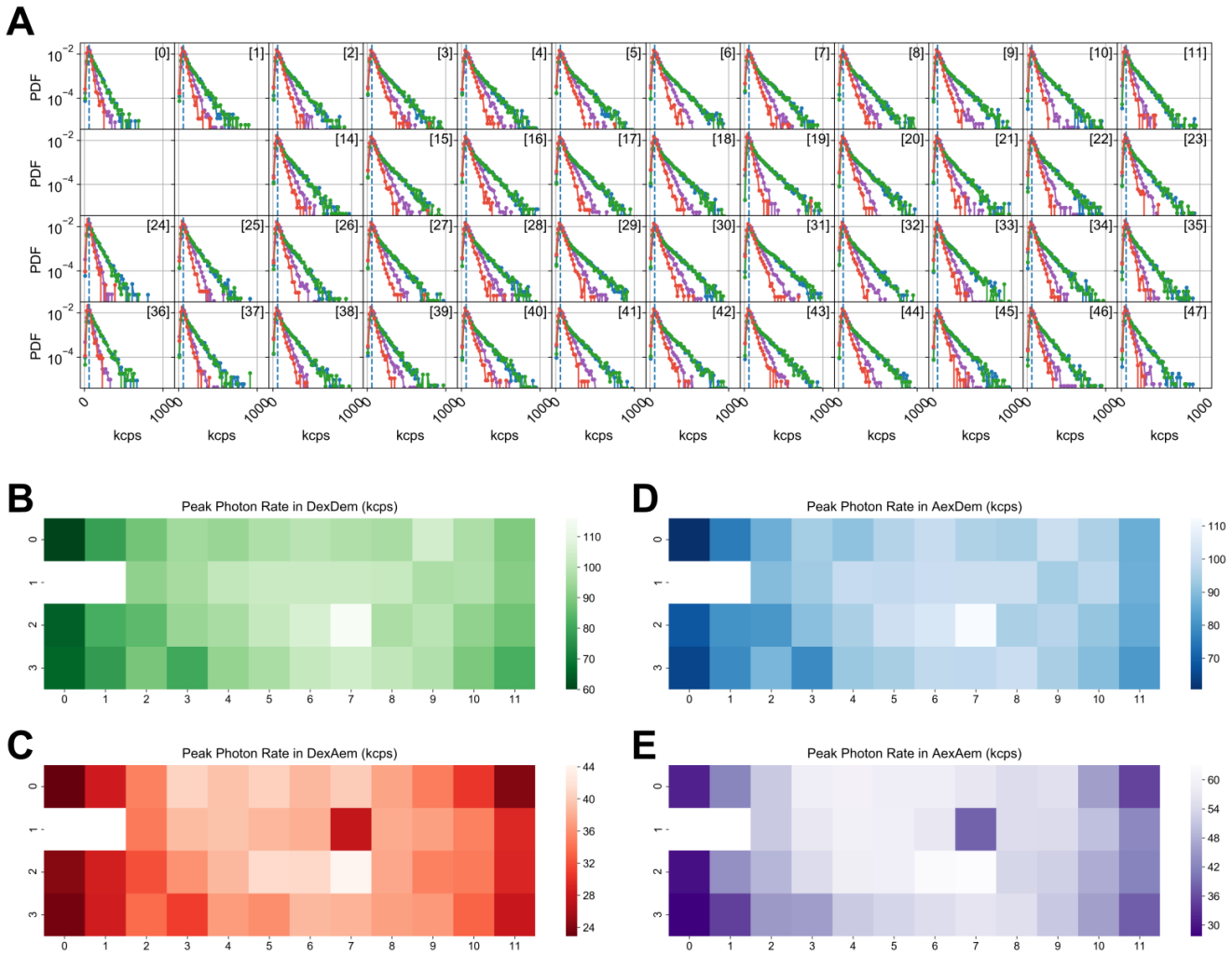


Figure 4. Peak photon rates in each of the 48 spots for a dsDNA sample with D-A separation of 12bp. Panel A: full distribution of peak photon rates. Panels B-E: Mean of the peak photon rate distribution in different photon streams. Two lateral spots in the second row exhibit no signal because of two malfunctioning pixels in the D-SPAD array. Color-coding indicates different photon streams. Green $D_{ex}D_{em}$, red $D_{ex}A_{em}$, light blue $DA_{ex}D_{em}$, purple $DA_{ex}A_{em}$. For more details see the notebook smFRET-PAX_single_pop-2017-05-23_08_12d.

bursts are detected in the lateral spots. While this effect decreases the overall maximum reachable throughput, it does not influence the uniformity of the ratiometric quantities $E_{PR}$ and $S$ across different spots. Conversely, in Fig. 4 (Panels C, E), we observe that the pixel at position (1, 7) in the A-SPAD array systematically detects fewer photons, an effect ascribed to a lower PDE of that pixel. This effect causes a bias in $E_{PR}$ and $S$ quantities as shown below.

Fig. 5 shows the distribution of peak photon rates obtained with the µsALEX setup. Comparing Figs. 4 Panel A and 5 it is clear that reduced sensitivity in the A-SPAD array results in lower peak photon rates in the $D_{ex}A_{em}$ (red) and $DA_{ex}A_{em}$ (purple) streams in the 48-spot setup.

### C. E-S histograms

After the initial burst search, it is necessary to apply a burst selection criterion to reject the smallest burst which dominates the distribution. Fig. 6 shows the E-S histogram for the dsDNA sample with D-A separation of 12bp, after selecting bursts with photon counts from all the streams larger than the threshold. We observe that D-only and FRET populations (respectively top left corner and center in the 2-D histogram) are clearly distinguishable in most channels. Moreover, as shown in Fig 7, it is easy to isolate the FRET population(s) by applying a burst selection on the $DA_{ex}A_{em}$ counts and on $D_ex$ counts. The separation of FRET from singly-labeled species is the primary advantage of dual laser excitation.

Without any further calibration, the spread across different channels is limited and does not affect the ability to distinguish subpopulations. This is evident in Fig. 8

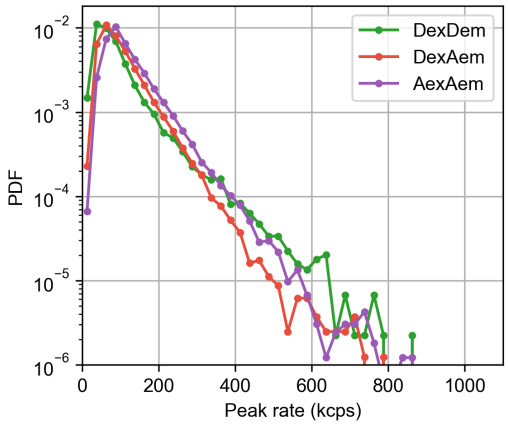


Figure 5. Distribution of peak photon rates in a single-spot µsALEX measurement of the dsDNA sample with D-A separation of 12bp. Color-coding indicates different photon streams. Green $D_{ex}D_{em}$, red $D_{ex}A_{em}$, purple $A_{ex}A_{em}$.For more details see the notebook us-ALEX_analysis-2017-06-11_000_12d.

which shows the $E_PR$ and $S_u$ peak center position in different spots for both D-only and FRET populations. Fig. 9 shows the center and $\pm 1\,\sigma$ range of fitted E-S peaks for the FRET population (blue dot and error-bar) for each channel. The orange dot is the mean center peak position of the FRET population across all the spots. We note that, for almost all channels, the deviation of the peak position is very well below the $\pm 1\,\sigma$ range, with exception of channel 19, where lower PDE of the A pixel causes a larger deviation from the peak position. In Fig. 8 and 9 we present results without channel calibration for the purpose of illustrating the raw performance of the system. It is possible, however, to reduce the channel-to-channel variations on E-S peak position by applying a per-spot calibration briefly described in the next section (with full details in appendix E). For comparison, the E-S histogram for a low-FRET dsDNA (D-A separation 22bp) is reported in appendix F, Fig. 13.

### D. Pooling data from all channels

To illustrate the high-throughput performance of the 48-spot system, we build an ALEX histogram accumulating bursts from all spots for a short time window of 15 s (Fig. 10). In principle, non-uniformities between different channels can be taken into account by decomposing $\gamma$ and $\beta$ in two factors: one that is an average value for all the spots and another that is a per-spot "relative" adjustment. The per-spot component of $\gamma$ and $\beta$ can be easily computed from a measurement of a static FRET sample (details in appendix E). Fig. 10, for simplicity and because of the good uniformity across spots, we report raw $E_{PR}$ and $S_u$ values without any spot-specific adjustments.

For comparison, Fig. 11 shows a similar histogram obtained by accumulating bursts for 15 s during a measurement of the same sample using the single-spot µsALEX setup. While we observe that the total number of bursts detected in the multispot measurement is about 12 times larger than in the single spot measurement, a quantitative comparison cannot be done because the measurements were taken on different dilutions in the two setups. Apart from the difficulty in controlling the sample concentration with high accuracy, there are other reasons why the burst number would not exactly scale with the number of spots. First, in the multispot setup, it is difficult to estimate the power in each spot because the intensity is not uniform and lateral spots receive less power. The power is calibrated such that, in the central spots, we obtain a signal in the D-channel comparable to the single-spot measurements (which used 180 µW @ 532 nm). The lateral spots receive less power and therefore detect a lower number of bursts. Second, the detection efficiency of the SPAD array in the red region of the electromagnetic spectrum is lower than that of the corresponding SPAD in the single-spot setup (see section II A), reducing total burst size and therefore the number of bursts selected with a given threshold.

## IV. CONCLUSION

We have described a new 48-spot single-molecule FRET setup designed for high-throughput single-molecule assays. Compared to our previous multispot setup[14], the number of spots was increased six-fold with a corresponding increase in throughput. While larger SPAD arrays have been demonstrated, they are fabricated using standard high-voltage CMOS processes resulting in poorer photon-counting performance than the custom technology process employed here. Convincing applications in cell FCS and FLIM, among others, have been published with these CMOS SPAD arrays[28–32], (for a comprehensive review see 33) but they remain a long way off from offering the sensitivity needed for single-molecule applications.

Compared to our previous works[14,34], a second alternating excitation laser was incorporated, and the corresponding alignment hurdles were solved, permitting sorting of single-molecules according to their D-A stoichiometry. In particular, we have shown that the setup allows identifying singly and doubly-labeled species over the full range of FRET efficiencies, opening the door to a much wider range of assays than was previously possible.

We presented a detailed description of the multispot setup and alignment procedure, which incorporates a number of technical solutions of potential interest for other applications. We also illustrated the smFRET measurement capabilities of the new setup using doubly-labeled dsDNA molecules as a proof of principle demonstration for sub-population separations and high-throughput measurements. Finally, we provided a comparison of its performance with that of a standard single-spot (confocal) µsALEX setup. Applications of this new instrument to the study of the initial stages of bacterial transcription and high-throughput diagnostics will be explored in future work.

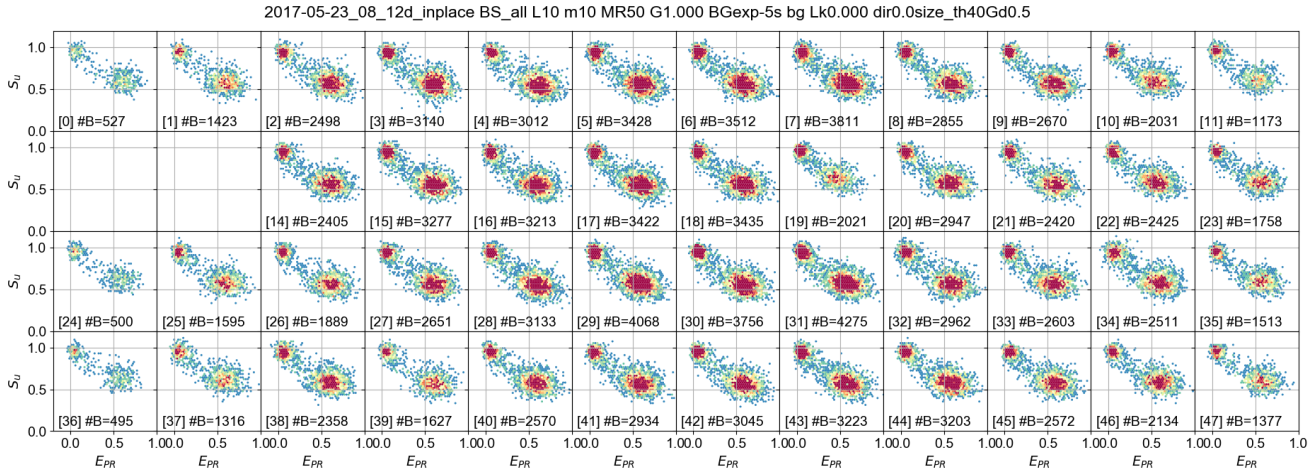


Figure 6. $E_{PR}$ versus $S_u$ histograms for the different spots in the dsDNA sample with D-A separation of 12bp. Two subpopulations are visible: D-only (around $E_{PR} = 0$, $S_u = 1$) and FRET population (around $E_{PR} = 0.6$, $S_u = 0.6$). Burst search was performed using all photons with constant-threshold burst search (50 kcps). Burst selection was performed on the total burst size after background correction, using a threshold of 40 photons. The legend in each subplot reports spot number ([·]) and number of bursts (#B).For more details see the notebook smFRET-PAX_single_pop-2017-05-23_08_12d.

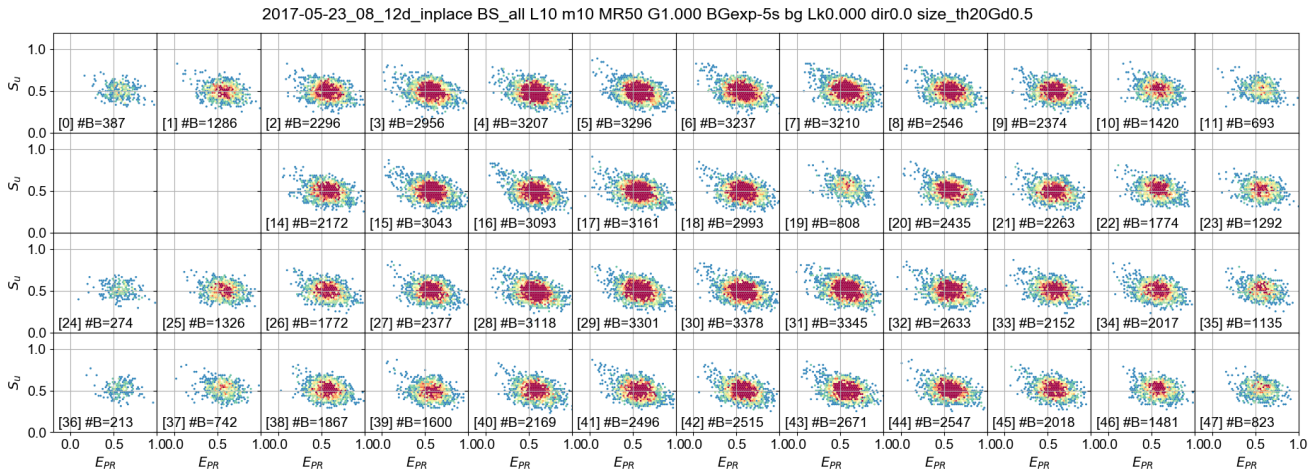


Figure 7. $E_{PR}$ versus $S_u$ histograms for the different spots in the dsDNA sample with D-A separation of 12bp. Data analysis and burst search are identical to figure 6, while burst selection was tailored to select only the FRET population: a burst is selected if the number of counts in the $D_{ex}DA_{em}$ and $DA_{ex}A_{em}$ streams are both larger than 20. The legend in each subplot reports spot number ([·]) and number of bursts (#B).For more details see the notebook smFRET-PAX_single_pop-2017-05-23_08_12d.

## ACKNOWLEDGMENTS

The authors thank Luca Miari for help in the initial stage of this project, Mr. Yazan Alhadid and Dr. Eitan Lerner for help with single-molecule sample preparation and Dr. Eitan Lerner for critical reading of the manuscript. We thank Dr. Bentolila for the generous loan of a LCOS SLM from the Advanced Light Microscopy/Spectroscopy Shared Resource Facility at the California NanoSystems Institute at UCLA. Research reported in this publication was supported by the National Institute Of General Medical Sciences of the National Institutes of Health under Award Number R01GM095904 & R01 GM069709, and by the National Science Foundation under Award Number MCB 1244175. The content is solely the responsibility of the authors and does not necessarily represent the official views of the National Institutes of Health or the National Science Foundation. Conflict of interest statements: S. Weiss discloses intellectual property used in the research reported here. The work at UCLA was conducted in Dr. Weiss's Laboratory. M. Ghioni discloses equity in Micro Photon Devices S.r.l. (MPD). No resources or personnel from MPD were involved in this work.

### Appendix A: Detailed setup description

The setup (Fig. 1) comprises two excitation CW lasers at 532 nm and 628 nm (2RU-VFL-Series, MPB Communications Inc., QC, Canada). For each laser, a half-wave plate and polarizing beam splitter are used for polarization and intensity control, as the polarization orientation must be aligned along the direction required by

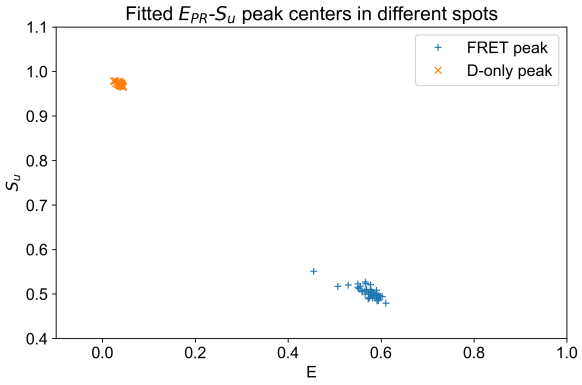


Figure 8. Scatter plot of the fitted $E_{PR}$, $S_u$ peak position in the different spots for the D-only (*orange cross*) and FRET populations (*blue plus*). Values were obtained by simple Gaussian fitting of the 1-D histogram of $E_{PR}$ and $S_u$ after a bursts selection that isolated D-only and FRET populations, respectively. For more details see the notebook smFRET-PAX_single_pop-2017-05-23_08_12d.

the LCOS-SLM. The 628 nm laser is directed through an acousto-optical modulator (P/N 48058 PCAOM, electronics: P/N 64048-80-.1-4CH-5M, Neos Technology, Melbourne, FL, USA) used for µs time-scale modulation, and the 532 nm laser is not modulated. Each laser goes through a first beam expander (Keplerian telescope, doublet lenses: 50 mm and 250 mm focal lengths). Two periscopes bring the beams to a raised optical breadboard where a microscope body (X71, Olympus Corporation, Japan) is fixed with its bottom port sitting over a circular aperture. Beyond the periscope, each beam goes through a second adjustable beam expander (3X, P/N 59-131, Edmund Optics Inc.). The red laser is reflected off mirrors $M1_R$ and $M2_R$ and phase-modulated by the "red" LCOS-SLM (P/N X10468-07, Hamamatzu, Japan), before passing through the dichroic mirror $D_{MIX}$. The green laser is reflected off $M3$, phase-modulated by the "green" LCOS-SLM (P/N X10468-01, Hamamatzu), and combines with the red excitation via the dichroic mirror $D_{MIX}$ (T550LPXR, Chroma Technology Corp, VT, USA). Both beams are recollimated by the $L_3$ lens (f=250 mm, AC508-250-A, Thorlabs) and focused into the sample by a high-NA objective lens (UAPOPlan 60x, NA 1.2, Olympus) after being reflected off the excitation dichroic mirror $DM_{EX}$ (Brightline FF545/650-Di01, Semrock Inc., NY, USA). The excitation pattern forms a dual-color 12x4 array of spots into the sample matching the geometry of the two SPAD arrays. The fluorescence emission is collected by the same objective lens, passes through the excitation dichroic $DM_{EX}$ and is focused by the microscope tube lens $L_2$ either on the side or the bottom port of the microscope. The side port mounts a sCMOS camera (Grasshopper3 GS3-U3-23S6M-C, FLIR Integrated Imaging Solutions Inc., BC, Canada) used during alignment while the bottom port redirects the beams toward the emission path. Here, a relay lens $L4$ (f=100 mm, AC254-100-A, Thorlabs) recollimates the image and sends it to an emission dichroic mirror $D_{EM}$ (Brightline Di02-R635, Semrock), which splits the signal into donor (D) and acceptor (A) spectral bands. The D path goes through a band-pass filter (Brightline FF01-582/75, Semrock) which removes residual 628 nm laser leakage and helps suppress Raman scattering from the 532 nm laser. Both D and A paths are refocused by lenses $L5_D$ / $L5_A$ (f=150 mm, AC254-150-A, Thorlabs) on two 48-pixel SPAD arrays[23] (denoted as D and A SPAD throughout the text).

Both SPAD arrays are mounted on 3-axis micro-positioners. The directions orthogonal to the optical axis (X-Y) are software-controlled via open-loop piezo actuators (actuators: Newport 8302; drivers: Newport 8752 & 8753; Newport Corporation, Irvine, CA, USA). The third axis (Z) has manual actuators as requirements on the Z directions are much less stringent than for the X-Y directions. The D-SPAD array has an additional stage for rotation about the optical axis, which is used to match the relative orientation of the SPAD arrays. Software for controlling the micro-positioners is available in the picomotor repository.

Each SPAD array module is equipped with an internal FPGA (Xilinx Spartan 6, model SLX150), a humidity sensor, and a USB 2.0 connection. The default FPGA firmware used in this work allows acquisition of low-resolution (10-100 ms) time-binned counts via the USB connection that is also used for humidity monitoring. In addition, a standard SCSI connector includes 48 independent outputs providing a pulse for every detected photon in each pixel[23]. The two SCSI ports are fed through a custom adapter to an FPGA-based acquisition board (FPGA board: PXI-7813R, rack: PXI-1000B, National Instruments, Austin, TX) which performs timestamping with 12.5 ns resolution in parallel on the 96 channels (task implemented in LabVIEW 2011 using the FPGA Toolkit, code available here). The FPGA board transfers data asynchronously to a host PC via an MXI-4 link to a custom acquisition program written in LabVIEW 2011 (MXI-4 link: rack board PXI-8331; PC board PCI-8331, National Instruments). The acquisition program also controls red laser alternation using a pulse generation board (PXI-6602, National Instruments), whose clock is synchronized with the timestamping FPGA board (PXI-7813R) through a common bus line on the rack (PXI-1000B).

In addition to the aforementioned acquisition program, the host computer runs a second LabVIEW 2011 program controlling the phase pattern on the two LCOS-SLMs. During alignment, the acquisition program communicates with the LCOS-control program to scan the positions of the LCOS pattern and assess the position of the SPAD arrays (see appendix B).

The raw binary data is saved together with a text-based metadata file containing measurement details that are used to create the final Photon-HDF5 file[35,36]. Once the measurement is saved on the host PC, the raw data is immediately transferred to a Linux-based workstation via 1 Gb Ethernet link. The second workstation automatically performs conversion to Photon-HDF5 and data analysis, leaving the host PC available for acquiring the next set of data. The scripts for data transfer conversion and analysis are available in the transfer_convert repository.

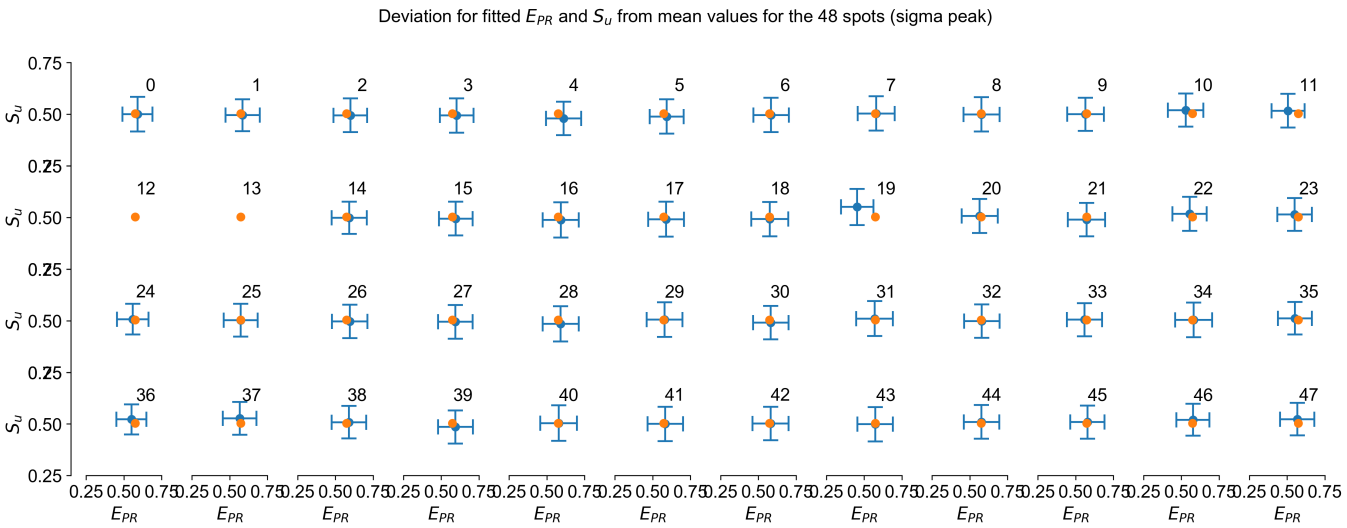


Figure 9. Fitted FRET peak position ($E_{PR}, S_u$, *blue dots*) and $\pm 1\sigma$ of the fitted Gaussian (*blue error bars*) for the 48 spots. As a reference, the mean $E_{PR}, S_u$ across the 48 spots (*orange dot*) is reported in each subplot. The spot number is indicated in the top right corner of each subplot.For more details see the notebook smFRET-PAX_single_pop-2017-05-23_08_12d.

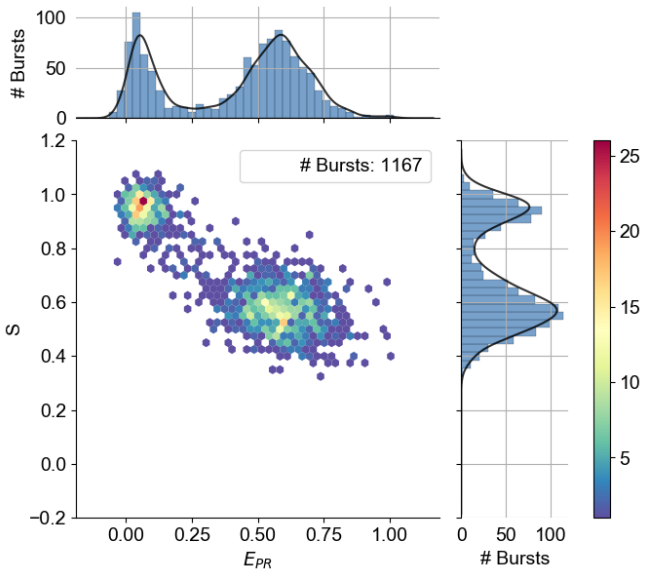


Figure 10. Multispot ALEX histogram obtained from 15 s of acquisition by pooling bursts from all 48 spots. For more details see the notebook smFRET-PAX_single_pop-2017-05-23_08_12d.

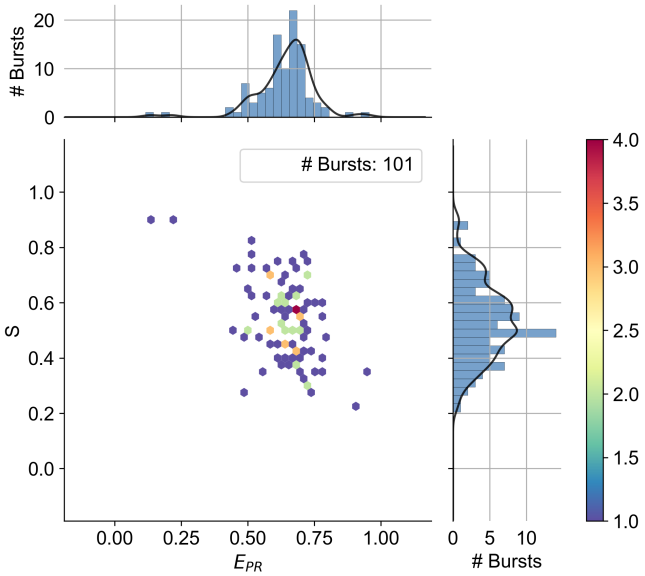


Figure 11. Single-spot ALEX histogram obtained from 15 s of acquisition for the same sample as in Fig. 10. For more details see the notebook us-ALEX_analysis-2017-06-11_000_12d.

## 1. LCOS-SLM Modulation

The array of 48 excitation spots is generated independently for each color by two LCOS-SLMs via phase modulation of an incoming plane wave, as previously described in 14 and 25. Briefly, the LCOS-SLM implements in direct-space the phase profile of a lenslet array that focuses an array of spots in a LCOS image plane at distances of 3-4 cm from the modulator surface (see Fig. 1). A rectangular region of the LCOS-SLM is subdivided into 12x4 adjacent blocks each implementing a single lens. The pattern can be adjusted by changing its center position, rotation, and X and Y pitch independently (operations equivalent to shifting, rotating or stretching the lenslet array). For both excitation wavelengths, the pitch and therefore the diameter of the lenslets is dictated by the detector geometry and by the magnification of the optical train from the LCOS-SLM to the detector. The spot pitch on the sample that nominally matches the detector geometry is 5.5 µm(500$\mu$m/90) in each direction, resulting in an LCOS-SLM lenslet pitch of 463 µm (23.1 LCOS-SLM pixels). This value is optimized during alignment to match the actual magnification and optical aberrations. Keeping the LCOS lenslets diameter and pitch constant, a change in the focal length results in a change

in NA and therefore spot size. The ratio of focal lengths in the two LCOS-SLM (32 mm for the red and 36 mm for the green) is chosen to compensate the difference in PSF sizes between 532 nm and 628 nm wavelengths.

The LCOS-SLM region surrounding the 12x4 pattern receives light that can can may result in stray "wide-field" excitation and therefore a strong background. For this reason, we fill the unused LCOS-SLM area with a "beam steering" pattern (a periodic pattern in one direction) that diffracts the incoming light at an angle with respect to the optical axis. This "steering" assures that light not contributing to the multispot patterns is not being collected by the back aperture of the objective lens. Additionally, the expanded laser beam is clipped by two rectangular apertures (slits) that are approximately 1 mm larger than the multispot pattern, further reducing light that otherwise contributes to background. This approach achieved low background without the need of an additional spatial filter as in our previous setup[14].

A similar approach for multispot generation is used in multi-confocal FCS from the Delon group[26]. An important difference is that they use a much longer LCOS focal length to construct a single phase pattern for all the spots (as the sum the contributions of each single spot). Conversely, in our approach, different portions of the LCOS-SLM are allocated to different spots. To the best of our knowledge, a detailed experimental comparison highlighting the relative strengths of these two approaches is currently lacking.

Software used to generate the multispot phase pattern used in this work is available in the lcos_multispot_pattern repository.

## Appendix B: Laser alignment

Each of the two lasers needs to be aligned in order to ensure (a) maximum uniformity between spot intensities (b) minimal aberrations across the patterns. To achieve (a) the Gaussian laser beam is expanded so that only the central part of the beam covers the excitation pattern (which has a maximum extension of 5 mm). To ensure (b), the geometrical center of the pattern needs to be placed on the optical axis.

In addition, (c) the excitation pattern of the two lasers must be aligned such that there is a maximum overlap between D and A excitation volumes for each spot.

### 1. Individual laser alignment

The 3X monolithic beam expanders have an adjustment ring used to control beam collimation. A simple way to ensure beam collimation is by sending the beam into the microscope through the excitation dichroic mirror, removing the external recollimation lens $L3$ and the objective lens, while placing a mirror on the sample holder and using the LCSO-SLM as a mirror i.e. with a constant phase pattern. Using the camera on the microscope output port, we adjust the collimation until a tight spot is formed. After adjusting the collimation, each beam must be aligned so that the peak intensity is at the center of the optical axis. To this end, without the recollimating lens $L3$, an iris $I2$ is placed before the beam enters the microscope side port. Using an aperture of 1-2 mm, only a narrow beamlet goes through the objective and generates a spot from the cover-glass reflection. Only when the input beam is parallel to the optical axis, the spot in the center of the field of view is assumed to be located in the center of the cross-hair in the microscope's eyepiece. In order to make the input beams parallel to the optical axis, the last mirrors before the microscope are adjusted ($M2_R$ for the red and $DM_{MIX}$ for the green laser). By defocusing the spot, we obtain symmetrically concentric patterns only if the input beamlet intersects with the optical axis at the back aperture of the objective lens. Since the direction is already fixed, we move the $I2$ iris to obtain the most radially-symmetric defocused pattern. In this way, the beamlet that goes through $I2$ coincides with the microscope optical axis. The last step is translating the input beam without changing its incidence angle until the intensity peak is aligned to the iris center. Alignment of beam direction and iris must be repeated until convergence. Once complete, both beams are parallel and concentric with the optical axis to a good approximation. When placing $L3$ a spot is formed at a different focus position. $L3$ can be aligned assuring that this new spot is in the same position as the spot obtained without $L3$.

### 2. Achieving overlap of the green and red patterns

Starting with the green LCOS-SLM, we project a multispot pattern into a highly concentrated solution of dyes (100 nM - 1 µM) used for alignment. Using a square grid of spots with an odd number of spots per side (i.e. 9x9) ensures that one spot is at the center of the pattern. The camera on the side-port detects an image of the pattern. The centering of the pattern with respect to the optical axis can be assessed from the amount of geometrical aberrations in the lateral spots. We center the excitation pattern by rigidly translating the pattern on the LCOS-SLM so that geometrical aberrations are roughly equivalent on the four sides. Next, we perform a 2-D Gaussian fitting of each spot, and from the distribution of sigmas and rotation of each Gaussian, we estimate a more accurate position of the optical axis (for the analysis see the notebook LCOS pattern fitting-conf9_G_conf14_R_4x12_slits). This step may be repeated multiple times until convergence. From this point on, the X-Y positions of the green LCOS-SLM is not changed anymore, and its center becomes a reference for the optical axis position.

Next, we activate the red LCOS-SLM and project a multispot pattern excited by the 628 nm laser. Using the camera, we align the red pattern to the green one used as a reference. An initial coarse adjustment of the red LCOS-SLM pattern is manually performed by observing the emission pattern on the live camera display. Then, the center position of the red LCOS-SLM pattern is finely adjusted by fitting the spot positions in the green and red images (Fig. 3), taken separately (the analysis notebook

can be found in multispot-software).

Finally, in order to reduce the background due to unmodulated light, two custom-made rectangular slits (aluminum with black finish) are added in the path before each LCOS ($S_R$ and $S_G$ in Fig. 1). The slits are aligned to illuminate only the 12x4 pattern (±1 mm) on the LCOS-SLM (see appendix A 1).

### Appendix C: SPAD arrays alignment

Both detectors must be aligned so that each pixel is optically conjugated to the corresponding excitation volume (excitation PSF). The goal is to have pairs of corresponding pixels on the two arrays detecting photons from the same sample volume (detection PSF). At the same time, in order to maximize the signal, the detection PSF must be concentric with the excitation PSF. Achieving this with a 2-D arrangement of spots and pixels requires not only aligning the X-Y position of the detectors, as in single-spot measurements, but also aligning the relative rotation of the two SPADs and adjusting the pitch and rotation of the excitation pattern to optimally match the detectors' geometry.

For alignment, we use a high concentration dye mixture (ATTO550, ATTO647N, ∼500 nM) excited by both lasers. With this sample, the 532 nm laser generates fluorescence signal in both D and A channels, while the 628 nm laser only generates a signal in the A channel. At this point, the position of both 532 nm and 628 nm excitation patterns on the LCOS-SLM has already been fixed in order to minimize geometrical aberrations as described in appendix B. Therefore, the excitation pattern position is used as the reference for aligning the SPAD arrays. Tyndall et al.[37] have presented an automatic procedure to align a LCOS-SLM multispot pattern to the detector. Here we align the SPADs to the LCOS-SLM pattern. Starting with the green laser only, both SPADs are manually positioned in X and Y to match the center of the excitation pattern. This is achieved by maximizing timetraces of SPAD counts displayed by the acquisition program while moving the detectors.

Next, we perform a more automated procedure for fine alignment referred to as "multispot scan". A multispot scan involves rigidly translating the multispot pattern on an LCOS-SLM (typically 4x4 spots) in discrete steps along two orthogonal segments, forming a cross path. At the same time, counts from a SPAD array are integrated for each pattern position over 300 ms. During a scan, each emission spot draws a cross path roughly centered on a SPAD pixel. A typical scan covers a range of 10 LCOS-SLM pixels with a step size of 0.4 and is performed sequentially in both X and Y directions. The counts acquired as a function of the LCOS-SLM position resemble a peak profile that is used to estimate the SPAD pixel center positions in LCOS-SLM coordinates. Averaging the SPAD pixel positions we obtain an accurate estimation for the center of the SPAD array. Ultimately, this procedure yields the offset of each SPAD array with respect to the ideal excitation pattern center. With this information, we move the SPAD arrays to the ideal X-Y position using software-controlled piezo micro-positioners. The sequence of multispot scan and SPAD array translation is repeated until convergence. Initially, the two SPAD arrays are aligned with respect to the green LCOS-SLM pattern (532 nm). Next, the position of the red LCOS-SLM pattern (628 nm) is fine-tuned to match the position of the A-SPAD array, and the D-SPAD array does not detect any signal with 628 nm excitation. The optimal position of the red excitation pattern is determined from a multispot scan performed with the red LCOS-SLM while counts are acquired with the A-SPAD array. After this, both red an green excitation patterns, and D/A-SPAD array positions are fixed, and the alignment is complete.

The whole fine alignment procedure is routinely performed at the beginning of each day of measurements and lasts about 30 minutes. Fig. 12 shows the fitted coordinates after fine alignment of the central 4x4 set of pixels in the D and A-SPAD arrays.

#### 1. Rotation and pitch adjustment

In the previous section, we outlined the general fine alignment procedure repeated daily when using the multispot setup. However, when building the setup, additional steps are necessary (a) to align the relative rotation of the two SPAD arrays, (b) to determine the best pitch in X and Y for the green and red excitation patterns, and (c) to optimize the SPAD position along the optical axis (Z).

To extract rotation and pitch information, we perform a multispot scan followed by an additional analysis step. Specifically, the set of X-Y positions of each SPAD pixel obtained from the scan is fitted to a rectangular grid. The fitted grid parameters are center position, pitch in X, pitch in Y, and rotation angle. Each SPAD array will have a different set of fitted parameters.

To adjust the rotation angle, one of the SPAD arrays (D) is rotated about the optical axis in order match the angle of the second SPAD, where the rotation angle of each SPAD is obtained from the scan fits. Once the orientations of two SPAD arrays match, the rotation stage is locked, ensuring long-term stability of the rotational angle.

Regarding the pitch, information from the scan fits is used to finely tune the X and Y pitch of the LCOS-SLM pattern that optimally matches both SPAD arrays. We observed X and Y pitch difference of 1-2% due to non-idealities due to stigmatism in the optical path.

### Appendix D: ALEX and PAX

In ALEX, two alternation periods $D_{ex}$ and $A_{ex}$ (respectively D or A excitation) and two detectors (D and A) are involved. This results in four basic photon streams named $D_{ex}D_{em}$, $D_{ex}A_{em}$, $A_{ex}D_{em}$, $A_{ex}A_{em}$, where the first symbol indicates the excitation period and the second the detection channel. The $A_{ex}D_{em}$ stream only contains background because there is no fluorescent emis-

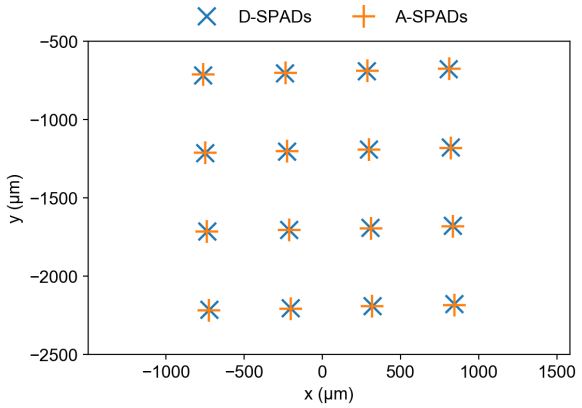


Figure 12. Experimental SPAD pixel coordinates after fine alignment for the D-SPAD and A-SPAD arrays. D-SPADs center positions are denoted by 'X' and A-SPADs center positions are denoted with '+'.

sion in the D-spectral band during A-laser excitation. For simplicity, we assume here that these quantities have been corrected for background[27].

A PAX setup has two detectors (D and A) but only one alternating laser (A). We define two periods, one when only the D-laser is on ($D_{ex}$) and one when both lasers are on ($DA_{ex}$). As in ALEX, combining the two excitation periods and the two detectors leads to four basic PAX photon streams: $D_{ex}D_{em}$, $D_{ex}A_{em}$, $DA_{ex}D_{em}$, $DA_{ex}A_{em}$. Formally, the only difference with the ALEX photon stream is that $A_{ex}$ in ALEX is replaced with $DA_{ex}$ in PAX. Differently from ALEX, however, all four photon streams in PAX contain useful fluorescent signal. In particular, $DA_{ex}D_{em}$ contains D-fluorescence due to D-laser excitation, while the corresponding term $A_{ex}D_{em}$ in ALEX contains only background. With this notation, in both ALEX and PAX, we can define the total fluorescence signal during D-excitation (e.g. burst size):

$$\Lambda = F_{D_{ex}D_{em}} + F_{FRET} \tag{D1}$$

where the $F$ quantities are background-corrected photon counts. $F_{FRET}$ is the A fluorescence due to FRET, computed by subtracting D-leakage and A-direct-excitation from $F_{D_{ex}A_{em}}$:

$$F_{FRET} = F_{D_{ex}A_{em}} - Lk\, F_{D_{ex}D_{em}} - Dir \tag{D2}$$

We also need the usual correction factors $\gamma$ and $\beta$[21]:

$$\gamma = \frac{\phi_A\, \eta^{A_{em}}_{A_{det}}}{\phi_D\, \eta^{D_{em}}_{D_{det}}} \tag{D3}$$

$$\beta = \frac{I_{A_{ex}} \sigma^{A}_{A_{ex}}}{I_{D_{ex}} \sigma^{D}_{D_{ex}}} \tag{D4}$$

where $\phi_A$, $\phi_D$ are the dye quantum yields and $\eta^{A_{em}}_{A_{det}}$, $\eta^{D_{em}}_{D_{det}}$ are the PDEs of the

D and A channels. In eq. D4, $I_{A_{ex}}$ and $I_{D_{ex}}$ are A and D-excitation intensities, while $\sigma^{A}_{A_{ex}}$ and $\sigma^{D}_{D_{ex}}$ are the dye absorption cross-sections at the respective laser wavelengths. $\beta$ accounts for the difference of D and A-dye fluorescence when each dye is excited by its respective laser.

We can define the $\gamma$-corrected total signal as[21,38]:

$$\Lambda_\gamma = \gamma\, F_{D_{ex}D_{em}} + F_{FRET} \tag{D5}$$

Differently from $\Lambda$, the quantity $\Lambda_\gamma$ does not change with FRET (as long as the dyes quantum efficiency does not change).

With these definitions, we can write the expression for proximity ratio $E_{PR}$ and FRET efficiency $E$ which is valid for both ALEX and PAX:

$$E_{PR} = \frac{F_{FRET}}{\Lambda} \tag{D6}$$

$$E = \frac{F_{FRET}}{\Lambda_\gamma} \tag{D7}$$

Conversely, the $S$ expression is slightly different for ALEX and PAX. In ALEX we define $S$ and the corrected version $S_{\gamma\beta}$ as:

$$S = \frac{\Lambda}{\Lambda + F_{AexAem}} \tag{D8}$$

$$S_{\gamma\beta} = \frac{\Lambda_\gamma}{\Lambda_\gamma + \frac{F_{AexAem}}{\beta}} \tag{D9}$$

The value $S_{\gamma\beta}$ is always centered around 0.5 for dual-labeled species, regardless of FRET efficiency or D and A-excitation intensities.

In PAX, we do not measure the $F_{A_{ex}A_{em}}$ directly, but we can compute it as:

$$\tilde{F}_{A_{ex}A_{em}} = F_{DA_{ex}A_{em}} - F_{D_{ex}A_{em}} \tag{D10}$$

By replacing $F_{A_{ex}A_{em}}$ with $\tilde{F}_{A_{ex}A_{em}}$, the PAX expressions for $S$ and $S_{\gamma\beta}$ become formally identical to eq. D8 and D9:

$$S = \frac{\Lambda}{\Lambda + \tilde{F}_{AexAem}} \tag{D11}$$

$$S_{\gamma\beta} = \frac{\Lambda_\gamma}{\Lambda_\gamma + \frac{\tilde{F}_{AexAem}}{\beta}} \tag{D12}$$

In PAX we can take advantage of the additional signal in $F_{A_{ex}D_{em}}$ and derive an equivalent set of PAX-enhanced expressions for $E$ and $S$. We can start extending the definitions of the total FRET signal of eq. D1 and D5 by including $F_{A_{ex}D_{em}}$ as follows:

$$\Lambda_{PAX} = F_{D_{ex}D_{em}} + F_{A_{ex}D_{em}} + 2F_{FRET} \tag{D13}$$

$$\Lambda_{\gamma,PAX} = \gamma\,(F_{D_{ex}D_{em}} + F_{A_{ex}De_m}) + 2F_{FRET} \tag{D14}$$

Based on eq. D13 and D14, we can write PAX-enhanced expressions for $E$ and $S$:

$$E_{PR,PAX} = \frac{2\,F_{FRET}}{\Lambda_{PAX}} \tag{D15}$$

$$E_{PAX} = \frac{2\,F_{FRET}}{\Lambda_{\gamma,PAX}} \tag{D16}$$

$$S_{PAX} = \frac{\Lambda_{PAX}}{\Lambda_{PAX} + \tilde{F}_{A_{ex}A_{em}}} \tag{D17}$$

$$S_{\gamma\beta,PAX} = \frac{\Lambda_{\gamma,PAX}}{\Lambda_{\gamma,PAX} + \frac{2\tilde{F}_{A_{ex}A_{em}}}{\beta}} \tag{D18}$$

Eq. D15, D16, D17 and D18 contain more photons than the classical expressions and, therefore, can result in lower shot-noise. However, this effect is mitigated by the fact that $F_{FRET}$ is counted twice to compensate for the doubling of the D signal and, therefore, its shot-noise is amplified.

### 1. Modified stoichiometry

By replacing $\tilde{F}_{A_{ex}A_{em}}$ with $F_{A_{ex}DA_{em}}$ in eq. D11, we define the "modified stoichiometry" $S_u$ used in this paper as:

$$S_u = \frac{\Lambda}{\Lambda + F_{A_{ex}DA_{em}}} \tag{D19}$$

This expression avoids the subtraction of photon counts (and the corresponding increase in shot-noise) necessary in PAX to compute $\tilde{F}_{A_{ex}A_{em}}$ (eq. D10). As a result, the $S_u$ distributions are tighter, permitting easier separation of FRET and D-only population. Note, however, that $S_u$ has a built-in dependency on the population FRET value, in particular $S_u$ decreases with the increasing $E$. In this work, even at low FRET values, better separation between FRET and D-only population was achieved using $S_u$ instead of $S$. In general, the preference of $S_u$ over $S$ may change in other PAX setups when the signal-to-noise and background-to-noise ratios are significantly higher. Once populations are separated, one can return using the classical $S$ expression for the purpose of computing gamma factors. Our interest, in the current paper, was not recovering absolute FRET values and D-A distances, but rather to demonstrate the capabilities of the smFRET-PAX system in terms of spot uniformity and throughput gain. Therefore, we did not compute a complete gamma factor calibration. However, we addressed the differences in collection and detection efficiency across different spots using a "relative" gamma coefficient $\chi_{ch}$ as illustrated in section E.

## Appendix E: Individual channel corrections

### 1. Gamma correction

The gamma-factor of each channel, $\gamma_{ch}$, can be expressed as the product of an average factor $\gamma_m$ and a spot-specific adjustment factor $\chi_{ch}$:

$$\gamma_{ch} = \gamma_m \cdot \chi_{ch} \tag{E1}$$

$\chi_{ch}$ can be easily computed from measurable quantities according to the following expression:

$$\chi_{ch} = \frac{\frac{1}{\langle E_{PR\,ch}\rangle_{ch}} - 1}{\frac{1}{E_{PR\,ch}} - 1} \tag{E2}$$

In eq. E2, $E_{PR\,ch}$ is the population-level proximity ratio for a specific channel, and $\langle E_{PRch}\rangle_{ch}$ is the average over all $N$ channels (in this case $N = 48$).

Eq. E2 follows from the following relation between $E$ and $E_{PR}$[21,38]:

$$E = f(E_{PR}, \gamma) = \frac{1}{1 + \gamma\left(\frac{1}{E_{PR}} - 1\right)} \tag{E3}$$

Solving eq. E3 for $\gamma$, we obtain:

$$\gamma = \frac{\frac{1}{E} - 1}{\frac{1}{E_{PR}} - 1} \tag{E4}$$

Formally, we can write $\gamma = \gamma_1\gamma_2$, where $\gamma_1$ is associated with a partially corrected proximity ratio $E_1$ as follows:

$$E_1 = f(E_{PR}, \gamma_1) = \frac{1}{1 + \gamma_1\left(\frac{1}{E_{PR}} - 1\right)} \tag{E5}$$

Writing $\gamma_1$ as a function of $E_1$ as in E4 and substituting the expression into eq. E3, we obtain $E$ as a function of $E_1$:

$$E = f(E_1, \gamma_2) = \frac{1}{1 + \gamma_2\left(\frac{1}{E_1} - 1\right)} \tag{E6}$$

Eq. E6 has the same form as E3 and E6. Therefore, $E$ can be obtained by two subsequent (chained) corrections for $\gamma_1$ and $\gamma_2$ respectively as in eq. E7.

$$E = f(E_{PR}, \gamma) = f(E_1, \gamma_2) = f(f(E_{PR}, \gamma_1), \gamma_2) \tag{E7}$$

In the multispot case, we apply this property to decompose the gamma correction into a spot-specific correction and an average correction as in E1. In particular, eq. E2 directly derives from E4 with simple substitutions.

### 2. Beta correction

Since, formally eq. D8 and D9 have the same form as $E_{PR}$ and $E$, we can write an expression equivalent to E3 for $S$ and $S_{\gamma\beta}$. Dropping the $\gamma$ subscript, we obtain:

$$S_\beta = \frac{1}{1 + \frac{1}{\beta}\left(\frac{1}{S} - 1\right)} \tag{E8}$$

Following the same arguments as in the previous section, the beta correction can be expressed as the product of a spot-average $\beta_m$ and an individual channel correction $\beta_{ch}$:

$$\beta = \beta_m \, \beta_{ch} \tag{E9}$$

Similarly to eq. E2, we can compute $\beta_{ch}$ as:

$$\frac{1}{\beta_{ch}} = \frac{\frac{1}{\langle S_{ch} \rangle_{ch}} - 1}{\frac{1}{S_{ch}} - 1} \tag{E10}$$

where $S_{ch}$ is the population-level non-beta-corrected stoichiometry ratio for a specific channel, and $\langle S_{ch} \rangle_{ch}$ is the average over all $N$ channels ($N = 48$ in this case).

### Appendix F: Additional data

Fig. 13 shows $E_{PR}$-$S_u$ histograms for the different channels obtained during the measurement of a 22d DNA sample (low-FRET). Due to the choice of donor and acceptor excitation powers during this measurement, the FRET population has an $S_u$ value larger than 0.5, artificially compressing the histograms in the upper part of the graphs. Nonetheless, it is still possible to distinguish FRET from D-only bursts, despite the low value of $E_{PR}$ for that sample, allowing a bias-free estimation of $E_{PR}$, as opposed to what would have happened in the absence of acceptor excitation[14].

## REFERENCES


[1] M. Dahan, A. A. Deniz, T. Ha, D. S. Chemla, P. G. Schultz, and S. Weiss, Chemical Physics **247**, 85 (1999).
[2] A. A. Deniz, M. Dahan, J. R. Grunwell, T. Ha, A. E. Faulhaber, D. S. Chemla, S. Weiss, and P. G. Schultz, Proceedings of the National Academy of Sciences **96**, 3670 (1999).
[3] T. Ha, A. Y. Ting, J. Liang, W. B. Caldwell, A. A. Deniz, D. S. Chemla, P. G. Schultz, and S. Weiss, Proceedings of the National Academy of Sciences **96**, 893 (1999).
[4] A. N. Kapanidis, N. K. Lee, T. A. Laurence, S. Doose, E. Margeat, and S. Weiss, Proceedings of the National Academy of Sciences of the United States of America **101**, 8936 (2004).
[5] M. Dimura, T. O. Peulen, C. A. Hanke, A. Prakash, H. Gohlke, and C. A. Seidel, Current Opinion in Structural Biology Carbohydrate–protein interactions and glycosylation • Biophysical and molecular biological methods, **40**, 163 (2016).
[6] B. Hellenkamp, P. Wortmann, F. Kandzia, M. Zacharias, and T. Hugel, Nature Methods **14**, 174 (2017).
[7] M. Hoefling, N. Lima, D. Haenni, C. A. M. Seidel, B. Schuler, and H. Grubmüller, PLOS ONE **6**, e19791 (2011).
[8] S. Kalinin, T. Peulen, S. Sindbert, P. J. Rothwell, S. Berger, T. Restle, R. S. Goody, H. Gohlke, and C. A. M. Seidel, Nature Methods **9**, 1218 (2012).
[9] A. Muschielok, J. Andrecka, A. Jawhari, F. Brückner, P. Cramer, and J. Michaelis, Nature Methods **5**, 965 (2008).
[10] A. Muschielok and J. Michaelis, The Journal of Physical Chemistry B **115**, 11927 (2011).
[11] J. R. Fries, L. Brand, C. Eggeling, M. Köllner, and C. A. M. Seidel, The Journal of Physical Chemistry A **102**, 6601 (1998).
[12] A. Ingargiola, R. A. Colyer, D. Kim, F. Panzeri, R. Lin, A. Gulinatti, I. Rech, M. Ghioni, S. Weiss, and X. Michalet, in *Proceedings of SPIE*, Vol. 8228 (SPIE, San Francisco, CA, USA, 2012) p. 82280B.
[13] A. Ingargiola, F. Panzeri, N. Sarkosh, A. Gulinatti, I. Rech, M. Ghioni, S. Weiss, and X. Michalet, in *Proceedings of SPIE*, Vol. 8590 (San Francisco, CA, USA, 2013) p. 85900E.
[14] A. Ingargiola, E. Lerner, S. Chung, F. Panzeri, A. Gulinatti, I. Rech, M. Ghioni, S. Weiss, and X. Michalet, PLOS ONE **12**, e0175766 (2017).
[15] A. N. Kapanidis, T. A. Laurence, N. K. Lee, E. Margeat, X. Kong, and S. Weiss, Accounts of Chemical Research **38**, 523 (2005).
[16] T. A. Laurence, X. Kong, M. Jäger, and S. Weiss, Proceedings of the National Academy of Sciences of the United States of America **102**, 17348 (2005).
[17] B. K. Müller, E. Zaychikov, C. Bräuchle, and D. C. Lamb, Biophysical journal **89**, 3508 (2005).
[18] N. K. Lee, A. N. Kapanidis, H. R. Koh, Y. Korlann, S. O. Ho, Y. Kim, N. Gassman, S. K. Kim, and S. Weiss, Biophysical Journal **92**, 303 (2007).
[19] S. W. Yim, T. Kim, T. A. Laurence, S. Partono, D. Kim, Y. Kim, S. Weiss, and A. Reitmair, Clinical Chemistry **58**, 707 (2012).
[20] S. Doose, M. Heilemann, X. Michalet, S. Weiss, and A. N. Kapanidis, European Biophysics Journal **36**, 669 (2007).
[21] N. K. Lee, A. N. Kapanidis, Y. Wang, X. Michalet, J. Mukhopadhyay, R. H. Ebright, and S. Weiss, Biophysical Journal **88**, 2939 (2005).
[22] A. Ingargiola, M. Segal, X. Michalet, and S. Weiss, Figshare (2017), m9.figshare.5146096, dOI: 10.6084/m9.figshare.5146096.
[23] A. Gulinatti, I. Rech, P. Maccagnani, and M. Ghioni, in *Proceedings of SPIE*, Vol. 8631 (SPIE, San Francisco, CA, USA, 2013) p. 86311D.
[24] X. Michalet, A. Ingargiola, R. A. Colyer, G. Scalia, S. Weiss, P. Maccagnani, A. Gulinatti, I. Rech, and M. Ghioni, IEEE Journal of Selected Topics in Quantum Electronics **20**, 1 (2014).
[25] R. A. Colyer, G. Scalia, I. Rech, A. Gulinatti, M. Ghioni, S. Cova, S. Weiss, and X. Michalet, Biomedical Optics Express **1**, 1408 (2010).
[26] M. Kloster-Landsberg, G. Herbomel, I. Wang, J. Derouard, C. Vourc'h, Y. Usson, C. Souchier, and A. Delon, Biophysical Journal **103**, 1110 (2012).
[27] A. Ingargiola, E. Lerner, S. Chung, S. Weiss, and X. Michalet, PLOS ONE **11**, e0160716 (2016).
[28] R. a. Colyer, G. Scalia, F. a. Villa, F. Guerrieri, S. Tisa, F. Zappa, S. Cova, S. Weiss, and X. Michalet, in *Proceedings of SPIE*, Vol. 7905 (SPIE, San Francisco, CA, USA, 2011) pp. 790503–790503–8.
[29] S. Burri, F. Powolny, C. Bruschini, X. Michalet, F. Regazzoni, and E. Charbon, in *Proceedings of SPIE*, Vol. 9141 (SPIE, Brussels, Belgium, 2014) p. 914109.
[30] J. Buchholz, J. W. Krieger, G. Mocsár, B. Kreith, E. Charbon, G. Vámosi, U. Kebschull, and J. Langowski, Optics Express **20**, 17767 (2012).
[31] M. Kloster-Landsberg, D. Tyndall, I. Wang, R. Walker, J. Richardson, R. Henderson, and A. Delon, Review of Scientific Instruments **84**, 076105 (2013).
[32] A. Kufcsák, A. Erdogan, R. Walker, K. Ehrlich, M. Tanner, A. Megia-Fernandez, E. Scholefield, P. Emanuel, K. Dhaliwal, M. Bradley, R. K. Henderson, and N. Krstajić, Optics Express **25**, 11103 (2017).
[33] C. Bruschini, H. Homulle, and E. Charbon, in *Proceedings of SPIE*, Vol. 10069 (SPIE, San Francisco, CA, USA, 2017) p. 100691S.
[34] A. Ingargiola, P. Peronio, E. Lerner, A. Gulinatti, I. Rech, M. Ghioni, S. Weiss, and X. Michalet, in *Proceedings of SPIE*, Vol. 10071 (SPIE, San Francisco, CA, USA, 2017) p. 100710Q.
[35] A. Ingargiola, T. Laurence, R. Boutelle, S. Weiss, and X. Michalet, in *Proceedings of SPIE*, Vol. 9714, edited by J. Enderlein, I. Gregor, Z. K. Gryczynski, R. Erdmann, and F. Koberling (SPIE, San Francisco, CA, USA, 2016) p. 971405, nIHMSID: NIHMS864335.
[36] A. Ingargiola, T. Laurence, R. Boutelle, S. Weiss, and X. Michalet, Biophysical Journal **110**, 26 (2016).
[37] D. Tyndall, R. Walker, K. Nguyen, R. Galland, J. Gao, I. Wang, M. Kloster, A. Delon, and R. Henderson, in *Proceedings of SPIE*, Vol. 8086, edited by P. T. C. So and E. Beaurepaire (2011) pp. 80860S–80860S–6.

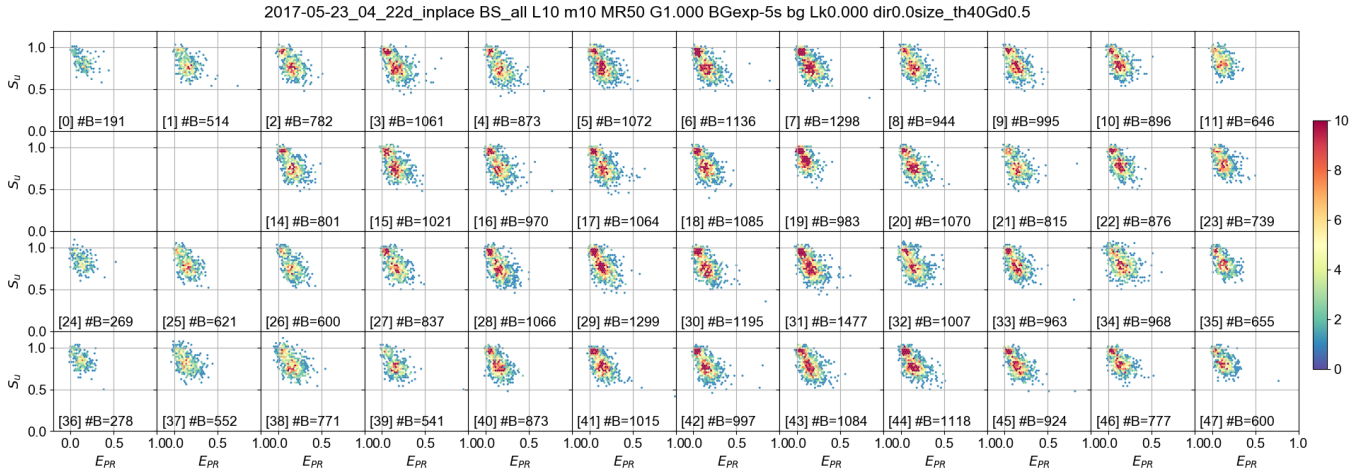


Figure 13. $E_{PR}$ versus $S_u$ histograms of all spots for the 22d dsDNA sample. Data analysis and burst search are identical as in figure 6. Burst search was performed using all photons with constant-threshold burst search (50 kcps). Burst selection was performed on the total burst size after background correction, using a threshold of 40 photons. The legend in each subplot reports spot number ([·]) and number of bursts (#B).

[38] A. Ingargiola, bioRxiv , 083287 (2017).
[39] S. Burri, Y. Maruyama, X. Michalet, F. Regazzoni, C. Bruschini, and E. Charbon, Optics Express **22**, 17573 (2014).
[40] I. M. Antolovic, S. Burri, R. A. Hoebe, Y. Maruyama, C. Bruschini, and E. Charbon, Sensors **16**, 1005 (2016).
[41] Y. Blancquaert, J. Gao, J. Derouard, and A. Delon, Journal of Biophotonics **1**, 408 (2008).